



3D Minimum Channel Width Distribution in a Ni-Base Superalloy

Moritz Müller¹ · Bernd Böttger² · Felix Schleifer¹ · Michael Fleck¹ · Uwe Glatzel¹

Received: 8 November 2022 / Accepted: 23 December 2022 / Published online: 17 January 2023
© The Author(s) 2023

Abstract

The strength of a Ni-base superalloy depends strongly on its microstructure consisting of cuboidal γ' precipitates surrounded by narrow channels of γ matrix. According to the theory of Orowan, a moving dislocation has to crimp through the minimal inter-precipitate spacing to admit the plastic deformation. We present a novel approach to evaluate the matrix channel width distribution of a matrix/ γ' microstructure in binary representation. Our method relies on precise determination of the matrix/precipitate interfaces and requires no additional user input. For each matrix channel between two neighboring precipitates, we identify the minimal interface to interface distance vector with its length being the channel width. The performance of this method is demonstrated on the example of the commercial alloy CSMX-4. We show that, in contrast to conventional line sectioning approaches, the approach consistently handles experimental 2D micrographs and 3D phase-field simulation data. The identified distance vectors correlate to the underlying crystal symmetry independent of the image orientation. The obtained channel width distributions compare well between the 2D and 3D data. This is in terms of similar median and σ of a log-normal distribution. The presented method overcomes limitations of the conventional line slicing approaches and provides a versatile tool for automated microstructure characterization.

Keywords Automated image analysis · Quantification of microstructure · Feature extraction · γ/γ' -microstructure · Ni-Base superalloys · Channel width

Introduction

Superalloys are the material of choice regarding high temperature and high mechanical stress environments. Typical applications are turbine blades in jet engines and stationary gas turbines. The efficiency of turbines is improved by increasing the turbine entry temperature, leading to growing demands on the materials. Superalloys and their manufacturing processes thus need to be optimized to further improve mechanical stability at higher temperatures. Typically, γ/γ' Ni-base superalloys are found in such applications. They consist of a face centered cubic (fcc) Ni solid solution matrix phase (γ) containing $L1_2$ ordered coherent precipitates (γ'). This microstructure leads to high strength at high homologous temperatures due to different mechanisms influencing the dislocation movement and stabilizing the microstructure.

This work will focus on the Ni-base superalloy CMSX-4, but the same γ/γ' microstructure is also found in Co-base and Pt-base superalloys, as well as compositionally complex alloys, where similar mechanisms are utilized to improve high temperature strength [1–3].

The extent of strengthening depends on the morphology of the γ/γ' microstructure which can be described by distributions of key microstructure parameters, such as precipitate sizes d and the channel widths L , that are the inter-precipitate spacings. Instead of distributions, mean or median values are often used as a model input, which could be improved upon by using distributions directly. Connected with these two distributions, the γ' volume fraction $V_{\gamma'}$ is another influence parameter. The relationship between the precipitation microstructure of γ/γ' Ni-base superalloys and its mechanical properties, such as the yield strength [4–8] or creep resistance [9, 10], is topic of many research works. The total influence of the precipitates is split into multiple mechanisms, relating to different dislocation-precipitate interactions. Considered are the lattice parameter misfit between the two coherent phases, leading to coherency stresses, as well as the anti-phase

✉ Uwe Glatzel
uwe.glatzel@uni-bayreuth.de

¹ Metals and Alloys, University of Bayreuth,
Prof.-Rüdiger-Bohrmann-Str. 1, 95447 Bayreuth, Germany

² Access e.V., Aachen, Germany

boundary shearing mechanism, when a dislocation shears a $L1_2$ ordered γ' precipitate. These contributions depend on the γ' phase volume fraction $V_{\gamma'}$ and the distribution of γ' precipitate sizes d , respectively.

The focus of this work is on the experimental and simulated determination of the minimal matrix channel width distribution L . This distribution is relevant when predicting the strengthening contribution through the Orowan mechanism as described in the following equation [11]

$$\tau_{\text{Oro}} = \frac{Gb}{L}, \quad (1)$$

where G is the shear modulus and b the magnitude of the Burgers vector. The shear stress τ_{Oro} must be exceeded for a dislocation to thread and bend through the spacing between two precipitates. The dislocations do not cut through the precipitates by shearing, but rather pass by the precipitates by bowing through the narrow matrix channels, as long as the local stress state is too small to shear the γ' precipitates. The passing of a narrower matrix channel involves an increased dislocation bending, that is energetically costlier and thus requires τ_{Oro} to be larger. Considering the path of a dislocation through a particular channel within an extended microstructure, the dislocation bowing is maximized at the place of minimal channel width. Therefore, if precipitate shearing can be excluded, it is the minimal matrix channel width L in the glide plane, which determines the total energy barrier height for the dislocation to pass that particular channel.

Within the extended microstructure the dislocations always choose the path of minimal resistance through all the different matrix channels. However, in conventional models, the mechanical behavior of precipitate strengthened alloys is usually described in terms of the mean channel width L_{mean} or the median value L_{50} of a measured

distribution. The distribution of channel widths plays a critical role in the temperature-dependent plastic deformation. When the channel widths show a very narrow distribution, for a dislocation every channel is equally costly to cross. The external stress required for dislocations to move through the microstructure can then be calculated by Eq. (1). A wider distribution of channel widths leads to a different picture. The external stress required to pass narrow channels is high and dislocations may choose to circumvent those obstacles by choosing a path through a wider channel. The total resistance of dislocation movement is becoming more of a serial and parallel connection of the stresses needed for the dislocations to pass through individual channels rather than a function of the mean values. For this reason, to classify the strength of a Ni-base superalloy based on its precipitate microstructure, information on the distribution of channel widths is crucial. [12, 13]

Channel width distributions need to be extracted from digital representations of the γ/γ' microstructure, which include micrographs from scanning electron microscopy (SEM) but also simulation results, often in the form of three-dimensional datasets. Techniques for extracting these microstructure parameters from such digital representations focus mostly on the analysis of micrographs. The goal behind all techniques is to achieve results with high accuracy, high reproducibility between different input images of similar content, and a high degree of automation, to allow for rapid evaluation of large datasets with as little human interaction and influence as possible. The last point goes hand in hand with reproducibility and comparability between similar data, as human bias and assessment are minimized.

Figure 1 shows the main steps in evaluating microstructure parameters starting from a greyscale SEM micrograph of the precipitation microstructure in a). The first step in

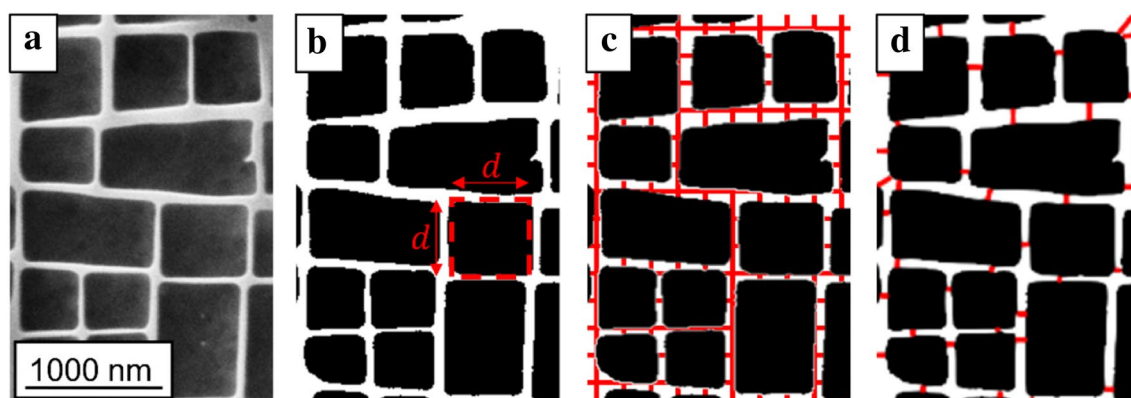


Fig. 1 **a** Section of a SEM micrograph depicting the γ/γ' microstructure of CMSX-4 in grey scale, **b** binarized representation of the section in **a**, with white pixels representing γ matrix, and black pixels representing γ' precipitates, the red dashed square indicates the

equivalent area-based method for evaluating precipitate sizes. **c** Visualization of line slicing for channel width analysis by horizontal and vertical lines only, **d** visualization of the minimal nearest neighbor distance channel width analysis

the microstructure analysis is to decide whether a certain image pixel belongs to precipitate or matrix. This step is called the image segmentation process and denotes a prerequisite for the subsequent quantitative image analysis, which is independent from the different methods for the image analysis discussed below. For distinguishing two phases this segmentation step is generally referred to as binarization, which is the denomination used in this work going forward. In Fig. 1 b) the result of a binarization step is shown, distinguishing between the two phases γ (white) and γ' (black).

Classically, the analysis of particle sizes from binarized images can be conducted using line-intersect methods [14, 15], which count the number of particles cut by a line laid over the image. Another option are chord-length analysis methods that lay vertical and horizontal lines through the image, counting consecutive pixels that were identified as the phase of interest. This method can be enhanced by evaluating more directions resulting in orientation dependent diameter distribution, as recently used by Kim et al. [16].

More commonly, particles completely surrounded by other phases are evaluated by measuring their area [17] or assuming a certain geometric shape and calculating e.g. the diameter of a circle, or the edge length of a cube with equivalent area [17–23], as indicated in Fig. 1b. Improved methods measure two diameters of ellipsoidal particles and therefore also evaluate the aspect ratio [24]. Taking the shape evaluation even further moment invariants can be used to quantify the shape of precipitates independent of orientation and size [25–27]. It was also shown that a quantitative comparison between 2D experimental and 3D phase-field particle shapes is possible using this method [27].

Figure 1c and d show the results of two different methods for evaluating the γ channel width distribution L based on the binary microstructure representation. Shown in Fig. 1c is the line slicing method, which is conducted along a certain orientation relative to the precipitate orientation [28, 29] or along two perpendicular directions in form of a grid [30, 31]. These techniques require knowledge about the orientation of the microstructure within the image to find a physically meaningful measure for the precipitate spacing that effectively hinders dislocation movement through a matrix channel. Additionally, the positioning and spacing of the individual lines need to be adjusted based on the precipitate size found in the image. Alternatively, errors that might arise from random placement, like the line coinciding with a parallel matrix channel, need to be corrected. This makes these methods difficult to fully automate. Figure 1d gives a glimpse of the performance of the method introduced in this work that is independent on the misorientation between the pixel grid of the binary data and the underlying crystallographic orientation. It renders a well-defined definition of the minimal channel width within the

viewed plane that relates to the inter-precipitate spacing that moving dislocations have to overcome.

Beside micrographs, we need to also analyze 3D simulation results using a consistently comparable method. These simulations are using the phase-field method. Phase-field simulations of microstructure evolution in general are frequently employed for the description and optimization of the physical and mechanical material behavior at mesoscale [32]. With respect to the present context, we mention the successful simulation application to the solidification of Ni-base superalloys [33–35] as well as to microstructure evolution during heat treatment [36–38]. Phase-field simulations operate with explicit microstructures, based on a diffuse interface description. In principle, the simulation results are very similar to segmented images from experimental micrographs. One important difference is the fact that phase-field simulations can be performed in the 3D space, thus providing 3D microstructural information. Further, the diffusive character of the γ/γ' interfaces impacts on the accuracy of the quantitative analysis of the simulations results. Depending on the width of the diffuse interface, we find systematic deviations in the resulting microstructure properties, such as the particle size [26]. By numerical resolution issues, conventional phase-field models require the diffuse interface width to be chosen at least four times larger than the grid spacing. This limitation can be overcome by advanced discretization techniques [39] or by employing the newly proposed sharp phase-field method, which allows the operation with interface widths on the scale of a single distance between two neighboring grid points [40, 41].

In this work we propose an automated procedure to consistently extract key parameters from both types of microstructure representations, 2D micrograph images and 3D simulation domains. More specifically, we focus on the evaluation of the matrix channel widths L . The procedure combines identifying nearest neighbor particles and finding their minimal distance into one step. It provides accurate statistical descriptions of L in form of distributions that can be used to predict mechanical properties, reducing the need for time and material intensive test series, and thus speeding up development of new alloys and processes. This is shown as an example for the alloy CMSX-4 for which micrographs and phase field simulations are readily available. The quality of the results of the new method is compared to respective results using conventional techniques such as slicing, or line intersect methods.

Methods

Experimental Microstructure Imaging

The alloy investigated in this work is CMSX-4. The corresponding chemical composition, as also used as simulation

Table 1 Composition of the alloy CMSX-4 in wt.% as used for simulation and experimentally measured by EDS

Element	Cr	Co	W	Al	Ti	Mo	Ta	Re	Hf	Ni
As simulated	6.5	9.0	6.0	5.6	1.0	0.6	6.5	3.0	0.1	bal
As produced	6.8	10.2	5.6	5.4	1.0	0.6	5.2	2.9	0.2	62.1

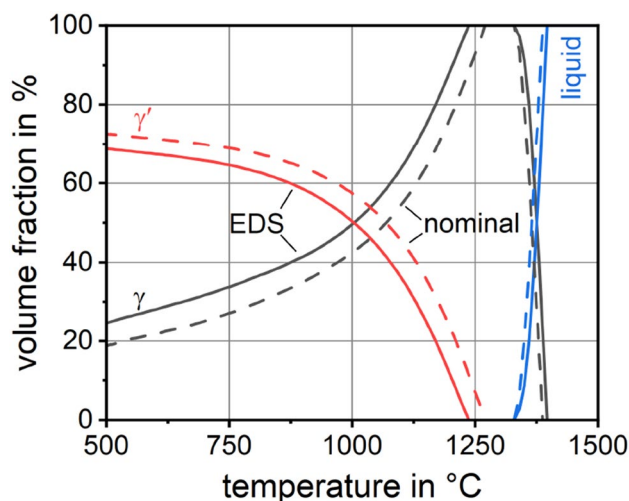


Fig. 2 Volume fractions V of the phases γ , γ' , and liquid in the CMSX-4 compositions “as simulated” (dashed) and “as produced” (continuous), as taken from Thermo-Calc

input parameter, is listed in Table 1. CMSX-4 is a second-generation single crystal (SX) Ni-base superalloy, which is characterized by the addition of 3 wt.% Re, leading to improved creep properties compared to first generation alloys such as CMSX-3 [11, 42–44]. After standard heat treatment, its microstructure is characterized by a γ' volume fraction $V_{\gamma'} \approx 70\%$ and a mean γ' precipitate size $d \approx 450$ nm [42, 45–48]. These values are optimal for achieving high creep strength at high temperatures, leading to a deformation mainly constricted to matrix channels [49, 50].

Experimentally, the specimen was prepared by alloying granules with a purity greater than 99.9%. High melting elements were prealloyed with Ni and then positioned in a ceramic crucible along with the remaining granule shaped elements [43, 44]. Following the Bridgman method, the constituents are molten and cast single crystalline in an induction vacuum furnace, as described in detail by Konrad et al. [51].

After the casting process the composition of the resulting specimen is analyzed on a cross section of the cylinder using a Thermo Noran System Six EDX-system with a Zeiss 1540ESB CROSS BEAM SEM. The composition of the cast single crystalline specimen was analyzed using EDS, the corresponding results are listed also in Table 1.

Figure 2 shows the results of ThermoCalc [52] calculations, that were conducted using the TCNI8 database,

analyzing the temperature dependent volume fractions of the γ and γ' phases for the two different compositions. The results confirm the suspected discrepancy in γ' volume fractions, likely due to the difference in Co and Ta content, leading to higher γ volume fractions. At the temperature of the second precipitation heat treatment step of 870 °C a $\Delta V_{\gamma'} = 65\% - 60\% = 5\%$ higher γ' volume fraction is predicted for the phase-field composition compared to the experimentally measured composition. This discrepancy is within the experimentally expected range.

The cylindrical specimen is oriented along the $\langle 100 \rangle$ directions, samples are then cut from it using electronic discharge machining. The samples are heat treated according to a standard heat treatment that includes a solution heat treatment step at 1320 °C for 2 h followed by an aging heat treatment step at 1140 °C for 6 h and a second aging step at 870 °C for 20 h [47]. After the solution step and the first aging step, the samples were air-cooled.

To prepare the heat-treated specimens for SEM microstructure imaging, they are embedded into an electrically conducting polymer resin filled with carbon (PolyFast, Struers). The surface is then prepared by first grinding using SiC paper with grit 320. Subsequently the sample is polished using 6 μm and 3 μm diamond suspension, followed by a final oxide polishing step using colloidal silica. The samples were then etched for 1 s using molybdc acid.

The γ/γ' microstructure micrographs are taken in a Zeiss SEM of type 1540ESB Cross Beam using the secondary electron detector (SE). An acceleration voltage of 20 kV was used in conjunction with an aperture of 60 μm and a working distance of 5 mm.

Figure 3a shows an exemplary micrograph of the alloy CMSX-4, that was used in the analysis. The square shaped γ' precipitates are clearly visible as the dark grey areas, separated by the light grey γ matrix phase. In Fig. 3b the corresponding result of the binarization using a deep convolutional neural net, based on the SegNet architecture [54], is shown. Here, black pixels represent the points inside a precipitate, white pixels the matrix phase points. This binarization has been performed, using the optimized neural network by Stan et al. [55], which was laboriously trained for this purpose [26]. The diagonal bands of matrix phase are also identified well. The neural net binarization shows some difficulty identifying precipitates, where the edge of the precipitate smoothly transitions into the matrix phase. All together the binarization result using the neural

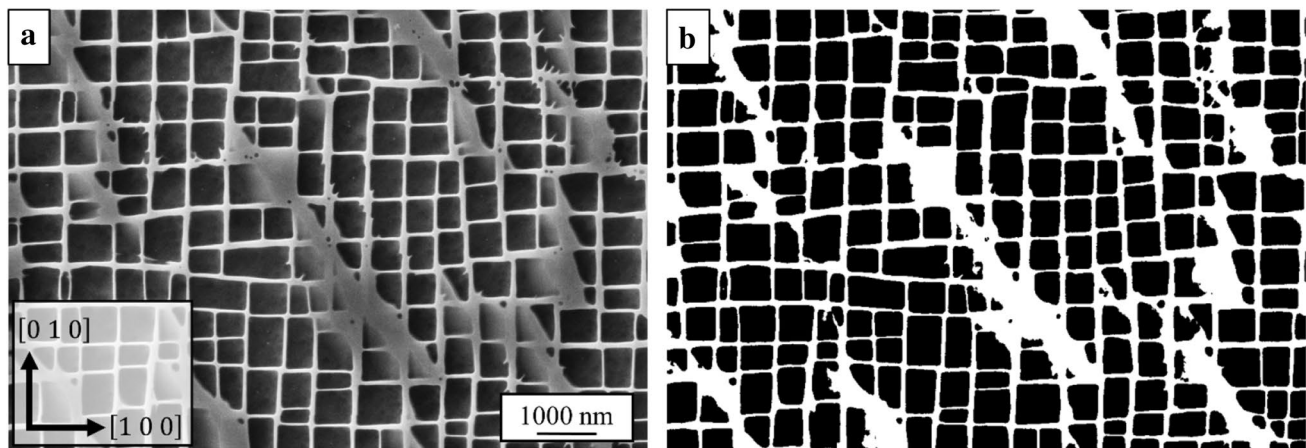


Fig. 3 Example of a CMSX-4 micrograph (a) and its segmentation result (b). In the segmented image, black pixels are inside γ' precipitates, and white pixels are γ matrix [53]

net delivers good performance and high reproducibility for the cost of time-consuming training.

In total we analyze 6 micrographs with a total number of 430 γ' precipitates. Their mean γ' area fraction is $F_{\gamma'} = 74\%$, from which a volume fraction of $V_{\gamma'} = 64\%$ can be estimated using [11]:

$$V_{\gamma'} = F_{\gamma'}^{3/2} \quad (2)$$

This assumes that the precipitates are perfect cubes. The γ' volume fraction of 64% lies between the ThermoCalc estimations for the nominal and measured composition of the material.

Phase-Field Simulation of Microstructure Formation

Phase-field simulations of Ostwald ripening and anisotropic coarsening (“rafting”) of the γ' phase in CMSX-4 have been performed using the software MICRESS® [56] following the aim to generate realistic 3D-microstructures for analysis. Within a 3D domain of $112 \times 84 \times 84$ grid cells with a resolution of $\Delta x = 0.02 \mu\text{m}$ and starting from pure fcc-phase with nominal alloy composition (Table 1), nucleation of γ' upon cooling, isothermal holding at 1140 °C for 6 h, and, finally, rafting at 950 °C under a uniaxial tensile stress of 185 MPa was simulated. By using a finite-differences correction scheme [39] the numerical interface thickness could be reduced to only 2.84 cells, leading to a significant reduction of simulation time in comparison to other phase-field models. During isothermal holding, due to the effects of elastic strain, cubic particles were formed. 3D-images were prepared based on the phase fraction of γ' . More details on the simulation parameters can be found in [57]. MICRESS® is a commercial software which uses a multi-component multiphase-field model [58] and which can be

online-coupled to arbitrary thermodynamic databases using efficient extrapolation methods [59]. Coupling to elastic stresses can be performed including mechano-chemical contributions [57]. These are of high importance in multicomponent high-alloyed systems like Ni-base superalloys and describe partial dissipation of elastic energy by stress-driven diffusion, generally leading to a reduction of the stress levels. The applicability of MICRESS® for scale-bridging and for simulation of process chains in ICME contexts has been recently demonstrated [38]. For the simulations, a difference in molar volume was assumed between the γ and γ' phases, leading to a lattice parameter misfit of $\delta \approx 0.17\%$, which is in good agreement with the experimentally determined value [37].

The microstructures of phase-field simulations are already segmented, as the phase-field variable φ describes, which phase is present at each numerical grid point. The γ' phase volume fraction can be easily evaluated by integrating over φ over the whole domain. This results in γ' phase volume fraction of $V_{\gamma'} = 60.7\%$, which is in good agreement with the Thermo-Calc prediction for the nominal composition of CMSX-4 at 950 °C (see Fig. 2). The mean precipitate size was evaluated to be $\mu_d = 440\text{nm}$ with a standard deviation of $\sigma_d = 170\text{nm}$, which is in good agreement to the distribution evaluated from the micrographs, featuring $\mu_d = 450\text{nm}$ and $\sigma_d = 170\text{nm}$.

Figure 4a shows the simulation domain colored according to the value of φ , where black represents the γ' particles at $\varphi = 1$ and white represents the γ matrix at $\varphi = 0$. The position of the boundary between γ and γ' phases at $\varphi = 0.5$ can be interpolated with higher than numerical grid accuracy [60]. This interpolation is applied to the so-called marching cube algorithm [61], to find the phase-field contour at $\varphi = 0.5$, that is then represented by a number of triangulated hulls. The resulting precipitate hulls are shown in Fig. 4b.

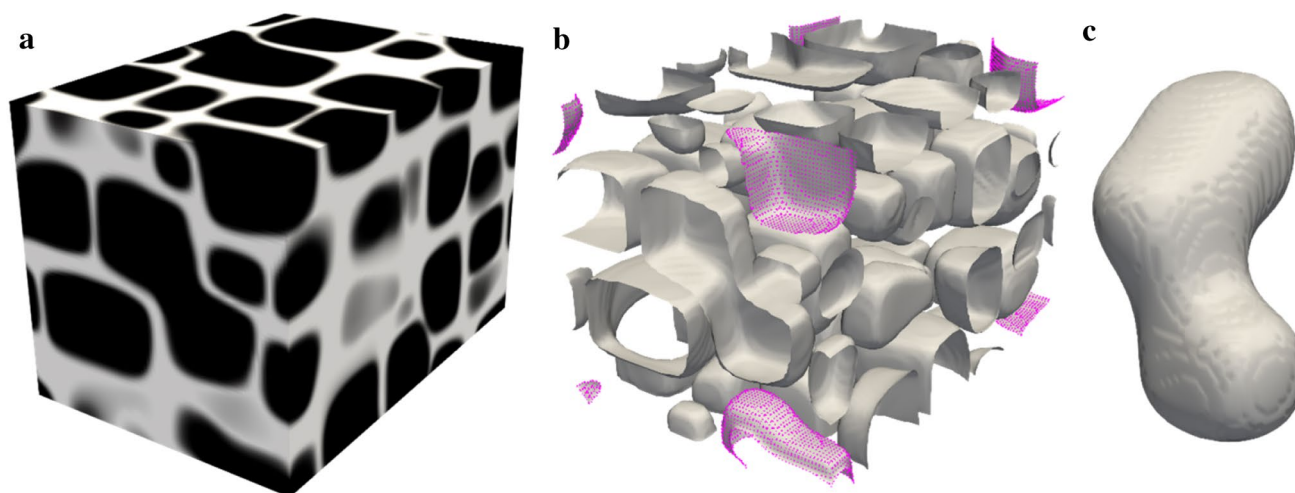


Fig. 4 **a** Plot of the phase-field variable ϕ on the surface of the simulation domain. Black indicates the γ' phase and white indicates the γ phase. Grey regions mark phase-field boundaries. **b** Plot of the γ' precipitate contour surfaces. The contour of a particle that crosses the

simulation domain is highlighted in pink. **c** Plot of the γ' precipitate contour surface of the precipitate marked in **b**, correctly combined considering the periodic boundary conditions

Next, a unique label is attributed to each individual particle in the domain. In this respect, the individual particles are defined through their contiguous areas/volumes for which $\phi > 0.5$ holds.

The size of each individual precipitate can be derived from its volume, which is calculated through the use of central moments as described in [62–64]. Due to the periodic boundaries of the simulation domain, particles that cross one or more of these boundaries are first recombined before their size is analyzed, as is exemplarily shown on the split precipitate marked pink in Fig. 4b and recombined in Fig. 4c.

Automated Channel Width Analysis

The microstructure analysis procedure described in the following sections is written in the Python programming language [65], making use of the open source packages scipy (v. 1.7.3) [66], numpy (v. 1.12.5) [67], scikit-learn (v. 1.0.2) [68], pandas (v. 1.4.1) [69, 70], and pyvista (v. 0.32.1) [71].

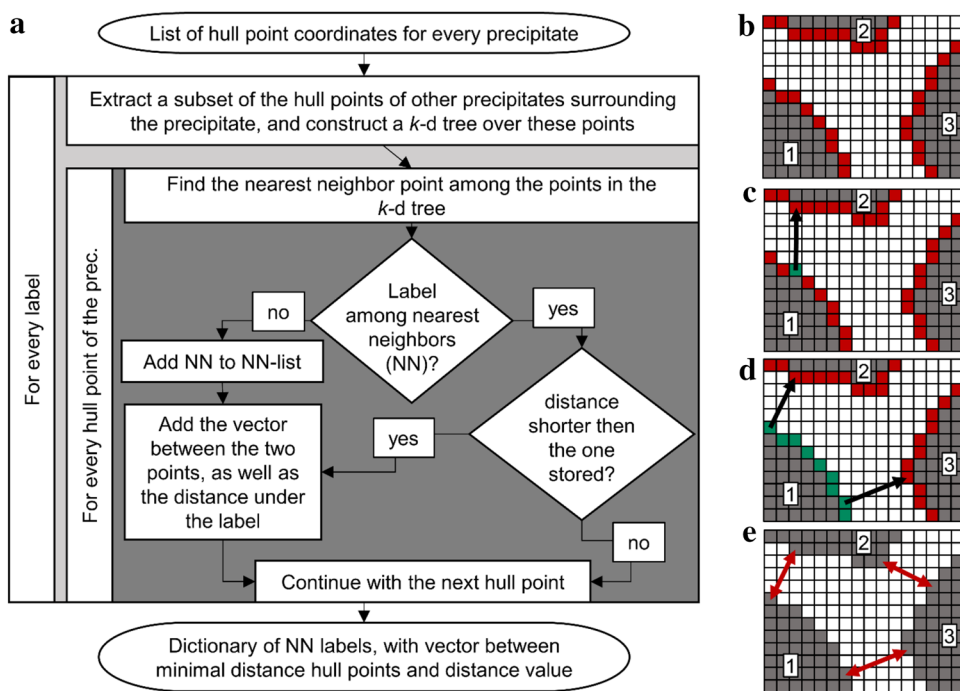
The first step in the evaluation of the channel width distribution L lies in finding the matrix/precipitate interfaces, also called the particle hulls. For the 2D pixel data from the micrographs, we define the hull points as all those precipitate points having at least one direct neighbor points that belongs to the matrix phase. Here, we restrict to the case of a two-phase microstructure only consisting of matrix-phase and the precipitate particles. For the 3D phase-field data, the hull points are already identified during the segmentation step.

Figure 5a shows the schematic of the algorithm that is used to identify the nearest neighbor (NN) particles and the minimal distance between them in a single step based

on the coordinates of all points on the particle hull, as indicated in the schematic in Fig. 5b. If we want to find the nearest neighbors of a certain particle P we extract a subset $S_{\text{local}} \subset S$ of all hull points surrounding P , where S represents all hull points. This reduces the number of points that need to be checked and thus increases the speed of the evaluation.

For every point on the hull of P we then find the nearest neighbor point among the points in the subset S_{local} created above. The computational effort to search scales linearly with the number of points N_P on the particle hull of P and the number of points in the subset $N_{S_{\text{local}}}$. To further improve the evaluation speed a so-called k -d tree as implemented in the python library scikit-learn [68] is employed, that finds the nearest neighbor for any point on the hull with an average time complexity of $O(\log N_{S_{\text{local}}})$. After a nearest neighbor point is found, as seen for the green pixel in Fig. 5c, we check if that neighbor has already been found before. If not, we add this particle as a new nearest neighbor, also storing the vector between the two points on the different particle hulls, as well as their Euclidian distance. If a nearest neighbor is already known, we check if the new distance is lower than the one already stored, and if that is true update the vector and Euclidian distance for this nearest neighbor particle. This results in a list of the nearest neighbor particles with the corresponding minimal particle distances in vector form and as the Euclidian distance. This is schematically shown in Fig. 5d) for the partial precipitate labeled “1”. If the procedure is repeated for all other precipitates, nearest neighbor precipitates and their minimal surface distances are identified (Fig. 5e)).

Fig. 5 a Flowchart for finding nearest neighbor (NN) particles as well as minimal distances between them, resulting in minimal channel widths of channels between neighboring precipitates. The figures on the right show a detailed state of an image after: **b** finding all pixels on the precipitate hull, **c** finding the nearest neighbor pixel on the hull of different precipitate, **d** finishing the iteration over the pixels on the surface of precipitate 1, **e** the algorithm has finished



Results and Discussion

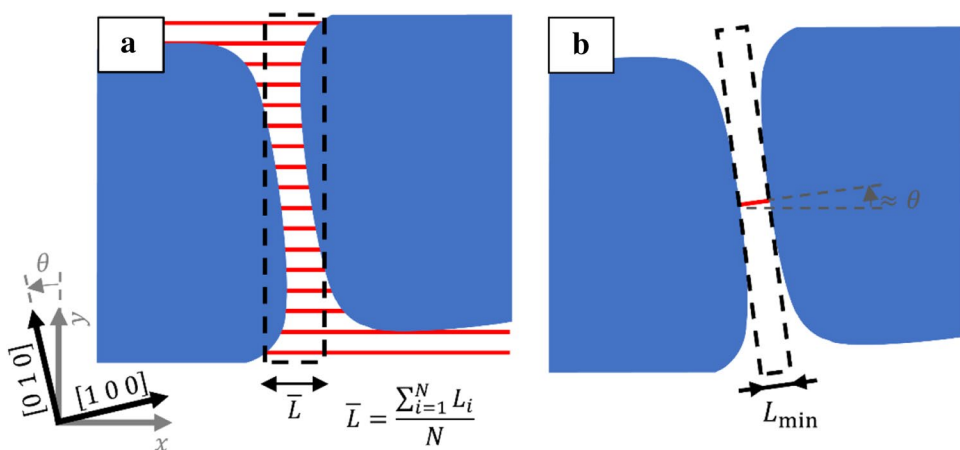
The developed algorithm for evaluation of the minimal channel width distributions from 2D micrographs and 3D phase-field simulation results is applied to both data types and compared to the result of a standard slicing analysis.

Channel Width Definition

Figure 6 schematically shows the difference between the evaluated channel width from the slicing method in part a and the here introduced minimal nearest neighbor channel width method in part b. In the schematic, the crystal $\langle 001 \rangle$ directions and therefore also the sides of γ' precipitates are

not perfectly oriented along the horizontal (x) and vertical (y) axes of the image. They differ from each other by a misorientation θ . The slicing method characterizes the channel width between two precipitates through multiple values in the directions of the image axes. This is represented by the red lines touching the two precipitates halves. The number of individual channel width values depends on the length of the channel and the distance between the slicing lines and is thus depended on a user input parameter that influences the resulting distribution. This means that the effectively measured channel width is a mean value over the channel length, and longer channels have a bigger influence on the overall distribution. Further, the misorientation between the crystal directions and the image’s pixel grid leads to an overestimation of the matrix channel width.

Fig. 6 Schematic drawing of the difference of the channel width evaluation by the slicing method (a) and by the newly introduced minimal nearest neighbor distance method (b). The coordinate systems shown in the bottom left indicates a misorientation θ between the crystallographic $\langle 100 \rangle$ directions of the material and the main coordinate directions x and y of the orthogonal grid, e.g. the pixel grid of a micrograph



In comparison, the minimal nearest neighbor distance method quantifies each channel with exactly one value, that is the minimal distance between two neighboring precipitates and that is independent of the misorientation between the image's pixel grid and the main crystallographic orientations. This leads to overall lower channel width values, where the measured distribution is shifted towards the left, as well as narrower distributions. There are no parameters that need to be specified beforehand and influence the resulting distribution.

Statistical Evaluation of Channel Width Distributions

The results of the evaluations are distributions of channel widths due to local differences in materials microstructure. Such distributions are most commonly represented in the form of histograms, where values are sorted into bins of a certain width and the number or relative frequencies for every bin is plotted on the y axis over the value range of the parameter on the x axis. The result of this kind of representation is strongly depended on how the bin size and the bin border positions are chosen, especially for distributions with a low number of values per bin.

All analysis methods for the channel width used in the following sections resulted in right skewed distributions that feature a longer tail towards higher channel widths values. It was found that the measured distributions are represented well by logarithmic normal distributions, which were fitted to the measured data using the Maximum Likelihood Estimation technique. The general form of the logarithmic normal distribution's probability distribution function f is given in Eq. (3), where L_{50} is the distributions median of L and σ_L is the standard deviation of $\ln(L)$.

$$f(L) = \frac{1}{L\sigma_L\sqrt{2\pi}} e^{-\frac{(\ln L - \ln(L_{50}))^2}{2\sigma_L^2}} \quad (3)$$

The mean of the channel width distribution L_{mean} and the mode of the channel width distribution L_{mode} can be calculated from L_{50} and σ_L according to Eqs. (4) and (5).

$$L_{\text{mean}} = e^{\ln(L_{50}) + \frac{\sigma_L^2}{2}} \quad (4)$$

$$L_{\text{mode}} = e^{\ln(L_{50}) - \sigma_L^2} \quad (5)$$

If ideal distributions are fitted to the data, the fit might look unsatisfactory when overlaid onto the histogram, but in reality, feature a very high coefficient of determination, which can be better seen in other representations. A trend corrected pp-plot was chosen to visualize the quality of the fits. Here the deviation of the fit from the measured

distribution, defined as the differences of the measured percentiles p_i and ideal percentiles of the fitted distribution t_i , are plotted over the measured quantiles q_i . The goodness of the fit is described by the distance of the points $(q_i, t_i - p_i)$ to the line $y = t_i - p_i = 0$. The smaller this distance is, the better the fit describes the data.

Channel Width Evaluation Results

Figure 7a and b show the qualitative results of the newly introduced minimal nearest neighbor distance method, where red lines indicate the identified minimal distance vectors between nearest neighbor particles. Another feature of this method can be identified when looking at the distributions of the misorientation angle between the distance vectors and the $\langle 100 \rangle$ directions of the crystal lattice, which are shown in Fig. 7c and d. It is clearly visible that the distance vectors are predominantly oriented in $\langle 100 \rangle$ directions without user input. This is an intrinsic feature of the algorithm that finds the minimal distance. In combination with the orientation of the cuboid precipitates, which's sides are oriented relative to the $\langle 100 \rangle$ crystal directions, this leads to an $\langle 100 \rangle$ orientation of the minimal distance vectors.

Figure 8 shows the results of the channel width analysis. The minimal nearest neighbor distance method is compared to the grid slicing method for both the 2D micrographs as well as the 3D simulation domain. The results of the micrograph analysis can be seen in Fig. 8a and c where the distributions resulting from the grid slicing and the minimal nearest neighbor distance method are shown as histograms. Note that the relative frequency on the y-axis is plotted logarithmically to better highlight the amount of large channel width values found by the evaluations. Both distributions show a skew towards high values and are represented well by logarithmic normal functions, as can be seen by the corresponding red lines overlaid onto the histograms and the high COD values of 0.93 and 0.99, respectively. There are clear differences noticeable between the two analysis methods applied to the micrographs that can be found in the histograms as well as the fits. The slicing result features a wider distribution, when looking at the histogram. A large number of channels wider than 500 nm are found using this technique. Reasons for this include the possibility of a slicing line being parallel inside a channel, as can be seen in Fig. 6a. Here a filter would be necessary to eliminate these incorrectly measured channel width values. The presented minimal distance method delivers results with a higher degree of relevance for microstructural evaluation without the need for manual post-processing. This can also be seen in Table 2, where statistical descriptors for the two methods are compared for both the original dataset as well as the logarithmic normal distribution fits.

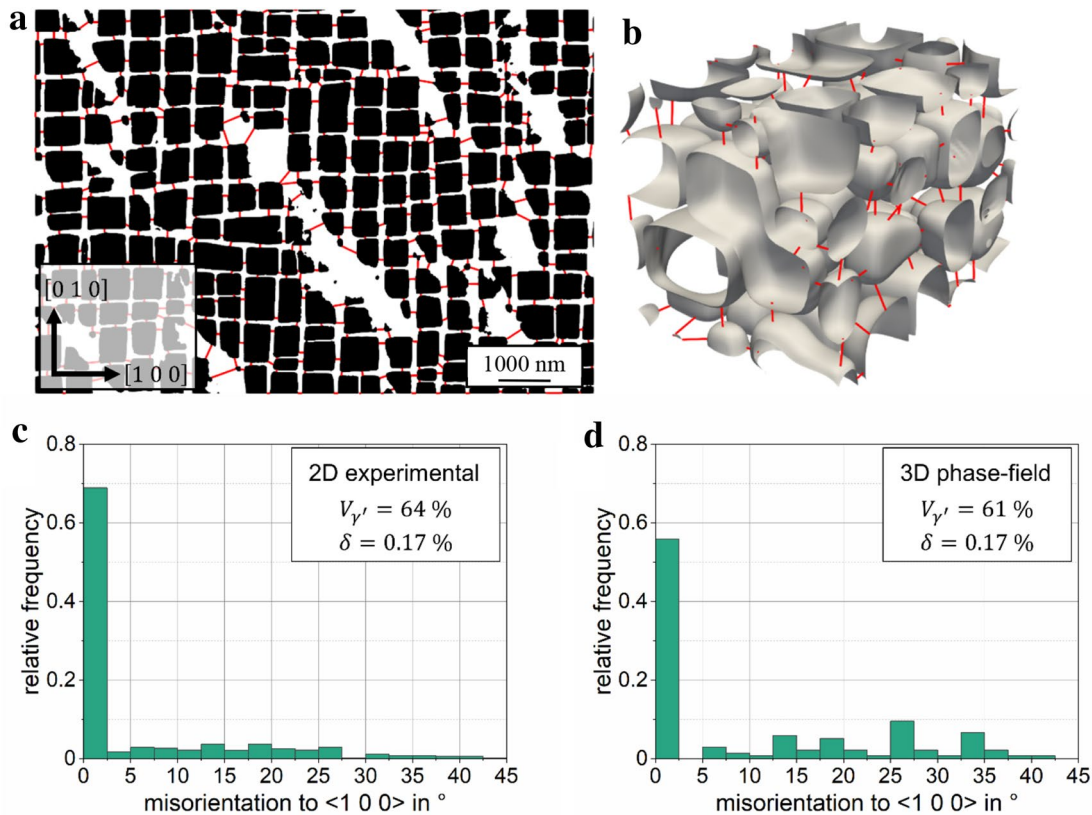


Fig. 7 Visualization of the channel width evaluation results using the minimal nearest neighbor distance method, where the minimal distance vectors for every channel are overlaid onto the segmented

micrograph **a**, and the $\varphi = 0.5$ iso-surface **b**, respectively. **c** and **d** show the distribution of the misorientation angles between the minimal distance vectors and the $\langle 100 \rangle$ direction

The median is often used to characterize non-symmetrical distributions. If we compare the median of the raw data of the two analysis methods, we find that the result of the slicing method is 18% larger. This can be explained by the random position a channel is evaluated at by the slicing line that does not necessarily coincide with the minimal channel width, as is shown in the schematic in Fig. 6a. The width is averaged over the whole length of the channel. Our method finds the minimal distance between the nearest neighbor precipitate hulls that make up a channel. In terms of the application of the channel width distribution data for the use in a model describing the microstructure dependent strength of an alloy, the minimal channel width in the glide plane is the critical value, as the Orowan strengthening contribution depends on L reciprocally, see Eq. (1), and therefore the smallest distance provides the maximum Orowan stress.

When we compare the quality of the fits of the logarithmic normal distribution to the histograms, we see that the result of the minimal nearest neighbor distance method is represented more accurately by a logarithmic normal function. This can also be seen in corresponding trend corrected pp-plot in Fig. 8e. A much lower discrepancy between

measured and fitted percentiles over the whole range of L can be seen for the minimal nearest neighbor distance method.

Figure 8b and d show the resulting distribution of channel width values for the simulation domain using grid slicing and minimal nearest neighbor distance method, respectively. Similar to the 2D result a skewed distribution of channel widths towards larger channels has been found in the 3D system. Again, a logarithmic normal function is fitted to the values, resulting in a good description of the measured distribution as proven by the trend corrected pp-plot in Fig. 8f. The result of the minimal nearest neighbor distance evaluation is better represented by the logarithmic normal distribution than the result of the slicing evaluation, which becomes also clear when comparing the corresponding coefficients of determination. Compared to our evaluation method, the slicing method results in a distribution with a much larger median value. Further, the two analysis methods result in significant differences regarding the width of the distribution, as can be seen by the statistical descriptors listed in Table 2. The effects that cause the distortion of the evaluation in 2D, namely misplacement and averaging, are further enhanced in the 3D case, as the chance for a slicing line

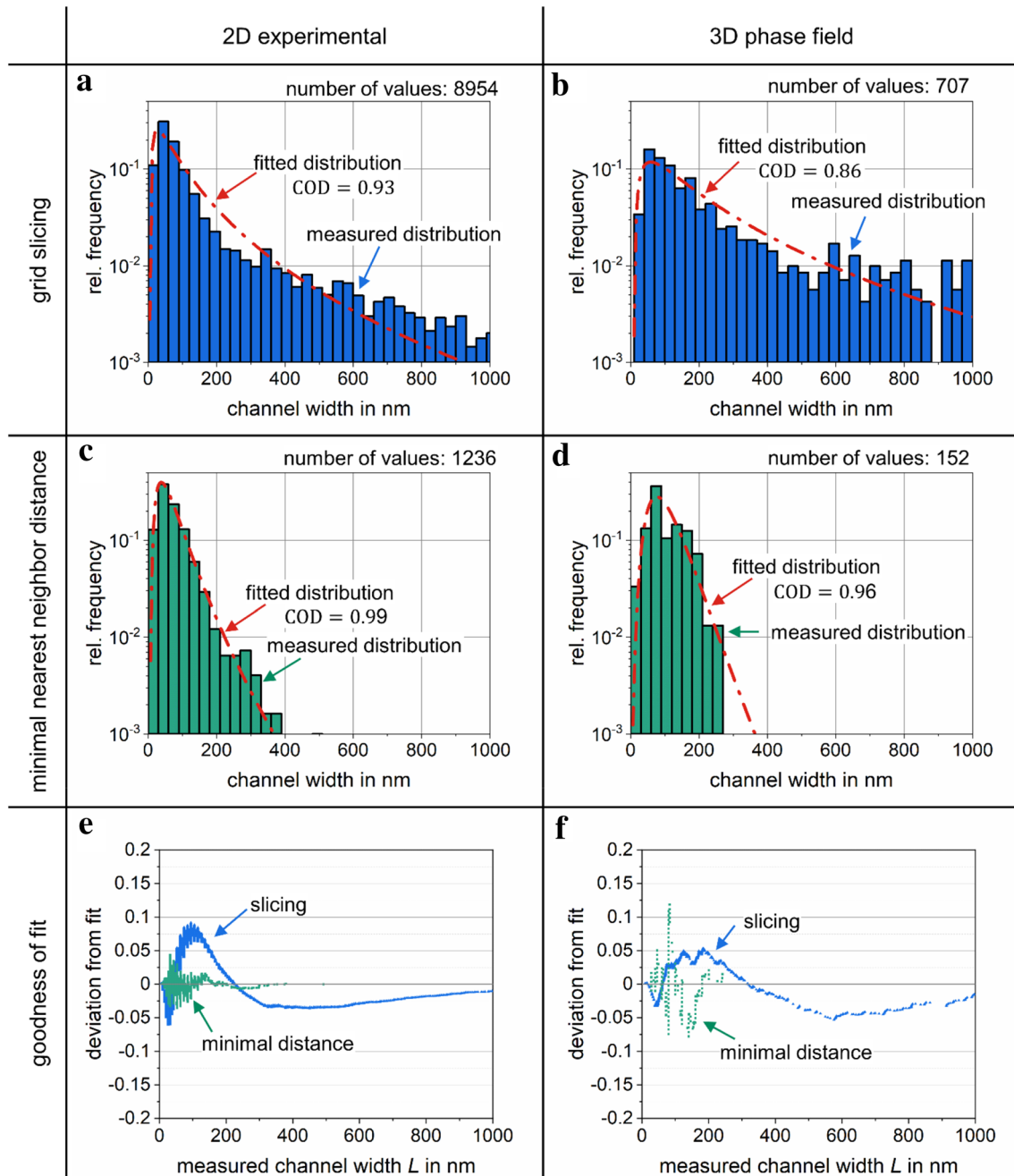


Fig. 8 Statistical results of the channel width analysis of: **a, c, e** six micrographs of CMSX-4; **b, d, f** a phase-field simulation domain of CMSX-4. **a, b, c, d** show the evaluation result presented as a histogram overlaid with the fitting result of a logarithmic normal distribution, the relative frequency is scaled logarithmically. **a** and **b** show

the results of a slicing measurement, **c** and **d** the result of the minimal nearest neighbor distance evaluation. **e, f** plot the relative difference between the measured and ideal percentiles over the measured quantiles, indicating the goodness of the fits

falling into a channel is higher, and the precipitates feature a more rounded shape which is likely caused by the interplay of lattice parameter misfit and interface energy [26].

The evaluated medians of the raw data and the fit distributions, as well as the mean channel width of the raw data distribution, are larger in the simulation than in the 2D micrograph.

For the slicing technique this difference amounts to a factor of 2.1 to 2.3, overestimating the 3D channel widths. Possible reasons for these differences include the higher temperature of 950 °C applied in the simulation, compared to the temperature of the last heat treatment step of 870 °C that the micrographs represent. This leads to a phase volume fraction lowered by

Table 2 Statistical descriptors of the channel width evaluations using grid slicing and the newly introduced method

		Raw data									Fits			
		Nr. of values	Min	L_{02}	L_{25}	L_{50}	Mean	L_{75}	L_{98}	Max	L_{50}	σ_L	COD	
Slicing	2D	8351	5.2	16	42	68	150	130	170	2800	83	1.1	0.93	
	3D	707	9.9	33	81	160	310	380	1300	2400	180	1.1	0.86	
Our method	2D	1236	7.4	16	37	58	73	95	250	490	59	0.7	0.99	
	3D	152	28	28	71	83	100	140	230	240	94	0.4	0.96	

The evaluations of raw data and logarithmic normal distribution fits are compared for 2D experimental micrograph and 3D phase-field simulation data. All values are given in nm

3%, thus resulting in larger channel widths for the simulation. The precipitate size distribution was found to be nearly identical for both 2D and 3D data sets. Further the γ' etching tends to also slightly etch away the γ channels, leading to lower values for the micrograph, again. Never the less, such a stark difference of more than factor two between simulations and experiments is not expected, as the phase-field simulations are sufficiently resolved to deliver accurate results, and the difference in $V_{\gamma'}$ of 3% is not large enough to cause these deviations. The results of the minimal nearest neighbor channel width method show differences of factor 1.4 to 1.6 using the same data base. This is a much-improved agreement between the 2D and 3D evaluation results. The differences between the median values of the fit and the raw data can be explained by the rather low number of channels present compared to the 2D investigation.

The presented method shows a couple of improved properties compared to the grid slicing method. The difference between the 2D and 3D channel width results is significantly smaller for the minimal nearest neighbor distance evaluation compared to the slicing method. The median channel widths differ by a factor of 1.5 rather than 2.3. Compared to the slicing method, our method evaluates the minimal channel width, rather than an averaged channel width, which could clearly be seen in the evaluated distributions. This minimal channel width in the glide plane is the parameter of interest, when quantifying the Orowan strengthening contribution. Further, the presented method can be fully automated, without the need for user input that would influence the resulting distributions and reduce reproducibility. This includes the orientation of the crystal lattice within the data set, which does not need to be known beforehand. Further, a filtering postprocessing step is not necessary. All in all, we see measured channel width distributions of high quality with high reproducibility.

Conclusion

We present a novel approach to evaluate the matrix channel width distribution in the γ/γ' microstructure of Ni-base superalloys. From a binary microstructure representation, the minimal surface to surface distance of two nearest

neighbor precipitates is evaluated without requiring additional input. This definition of the matrix channel width has a direct relation to the materials strength through the Orowan relation, as it corresponds to the inter-precipitate spacing that moving dislocations must overcome. Contrary to the common slicing method, every matrix channel in the data is represented by exactly one value. The strength of the presented approach was successfully demonstrated on the example of 2D micrographs and 3D phase-field simulation results, exemplified with the alloy CSMX-4. The slicing method finds significantly different channel width distributions when 2D and 3D data is compared. Slicing overestimates the channel width stronger in 3D than in 2D. The presented approach overcomes this limitation and shows significantly improved consistency as the obtained distributions from 2D experimental and 3D phase-field data compare very well both in terms of median channel width and shape of the distribution.

Outlook

The measured distributions of channel widths will be used to estimate the material strength contribution through the Orowan mechanism. Here distributions in the $\{111\}$ planes are of particular interest, as the slip system in Ni is $\frac{a}{2}\langle 110 \rangle \{111\}$ [11]. For the measured channel width distributions in $\{100\}$ planes, the distributions in $\{111\}$ planes can be estimated by multiplying the measured values by a factor of $\sqrt{3}/\sqrt{2} \approx 1.21$, which results from model calculations assuming perfect equisized cuboidal precipitates.

Figure 9 schematically shows how channel width distributions will be correlated to distributions of local Orowan stresses that need to be overcome for dislocation movement to proceed. This is done by scaling the measured $\{100\}$ logarithmic normal distribution, as shown in (a) in grey, to represent a distribution in $\{111\}$ planes, indicated by the red dashed line. The convolution of the resulting distribution with the relation of Orowan stress regarding to channel width, as depicted in (b) results then in a distribution of Orowan stresses, as is shown in (c). From this

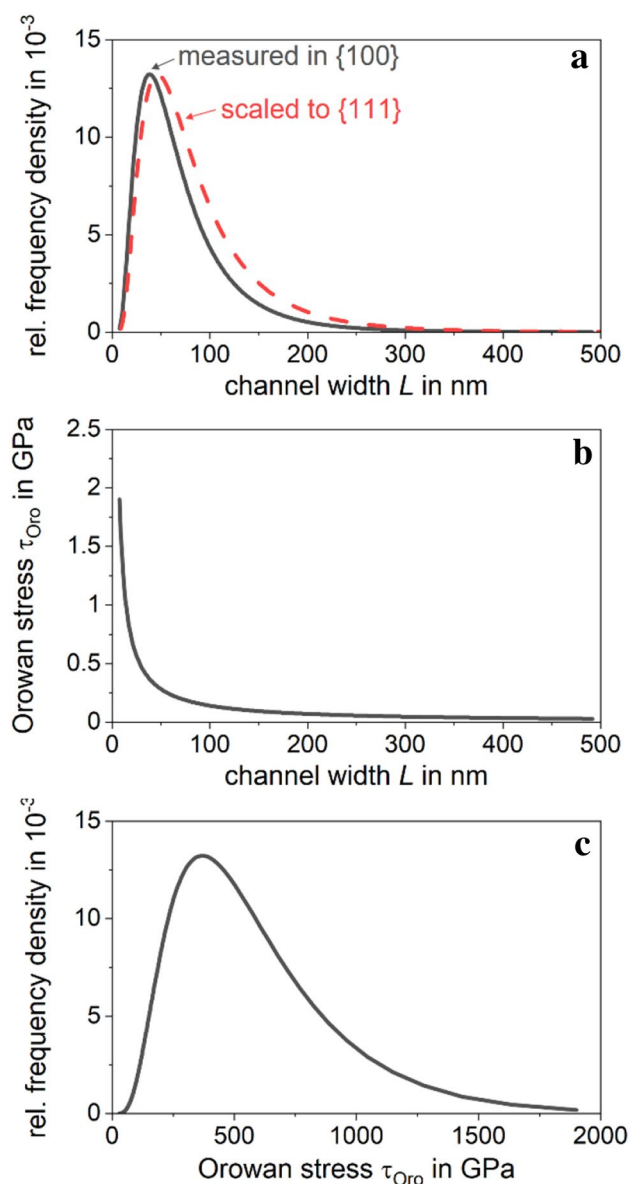


Fig. 9 **a** shows a schematic distribution of channel widths, represented by a logarithmic normal distribution; **b** shows the dependency of the Orowan stress on the channel width; **c** shows the distribution of Orowan stresses based on the channel width distribution in **a** and the Orowan Eq. (1)

distribution the material strength can be predicted in combination with other strengthening contributions.

Acknowledgements This work is funded by the Federal Ministry for Economic Affairs and Climate Action (BMWi) under the project SAPHIR (funding code: 03EE5049D) as well as by the German Research Foundation (DFG) in the framework of the Collaborative Research Center SFB-1120-236616214 “Precision Melting Engineering” and for the individual project no 394699463 under grant BO 4991_2-1.

Funding Open Access funding enabled and organized by Projekt DEAL.

Data Availability The presented data are available from the authors on reasonable request.

Declarations

Conflict of interest The authors declare that they have no conflict of interest.

Open Access This article is licensed under a Creative Commons Attribution 4.0 International License, which permits use, sharing, adaptation, distribution and reproduction in any medium or format, as long as you give appropriate credit to the original author(s) and the source, provide a link to the Creative Commons licence, and indicate if changes were made. The images or other third party material in this article are included in the article's Creative Commons licence, unless indicated otherwise in a credit line to the material. If material is not included in the article's Creative Commons licence and your intended use is not permitted by statutory regulation or exceeds the permitted use, you will need to obtain permission directly from the copyright holder. To view a copy of this licence, visit <http://creativecommons.org/licenses/by/4.0/>.

References

1. Suzuki A, Inui H, Pollock TM (2015) L1 2 -Strengthened cobalt-base superalloys. *Annu Rev Mater Res* 45:345–368
2. Haas S, Manzoni AM, Holzinger M et al (2021) Influence of high melting elements on microstructure, tensile strength and creep resistance of the compositionally complex alloy Al10Co25Cr-8Fe15Ni36Ti6. *Mater Chem Phys* 274:125163
3. Liebscher CH, Glatzel U (2014) Configuration of superdislocations in the γ' -Pt3Al phase of a Pt-based superalloy. *Intermetallics* 48:71–78
4. Galindo-Nava EI, Connor LD, Rae CMF (2015) On the prediction of the yield stress of unimodal and multimodal γ' Nickel-base superalloys. *Acta Mater* 98:377–390
5. Goodfellow AJ, Galindo-Nava EI, Christofidou KA et al (2018) The effect of phase chemistry on the extent of strengthening mechanisms in model Ni-Cr-Al-Ti-Mo based superalloys. *Acta Mater* 153:290–302
6. Kozar RW, Suzuki A, Milligan WW et al (2009) Strengthening mechanisms in polycrystalline multimodal nickel-base superalloys. *Metall Mater Trans A* 40:1588–1603
7. Ahmadi MR, Povoden-Karadeniz E, Whitmore L et al (2014) Yield strength prediction in Ni-base alloy 718Plus based on thermo-kinetic precipitation simulation. *Mater Sci Eng, A* 608:114–122
8. Li W, Ma J, Kou H et al (2019) Modeling the effect of temperature on the yield strength of precipitation strengthening Ni-base superalloys. *Int J Plast* 116:143–158
9. Glatzel U, Schleifer F, Gadelmeier C et al (2021) Quantification of solid solution strengthening and internal stresses through creep testing of Ni-containing single crystals at 980 °C. *Metals* 11:1130
10. Preußner J, Rudnik Y, Völkl R et al (2005) Finite-element modelling of anisotropic single-crystal superalloy creep deformation based on dislocation densities of individual slip systems. *Zeitschrift für Metallkunde* 96 Heft 96:595–601
11. Reed RC (2006) *The superalloys—Fundamentals and applications*. Cambridge University Press, Cambridge, UK
12. Rae C, Reed RC (2007) Primary creep in single crystal superalloys: origins, mechanisms and effects. *Acta Mater* 55:1067–1081

13. Kirchmayer A, Lyu H, Pröbstle M et al (2020) Combining experiments and atom probe tomography-informed simulations on γ' precipitation strengthening in the polycrystalline Ni-base superalloy A718Plus. *Adv Eng Mater* 22:2000149
14. Hays C (2008) Size and shape effects for gamma prime in alloy 738. *J Mater Eng Perform* 17:254–259
15. Nathal MV (1987) Effect of initial gamma prime size on the elevated temperature creep properties of single crystal nickel base superalloys. *Metall Mater Trans A* 18:1961–1970
16. Kim HN, Iskakov A, Liu X et al (2022) Digital protocols for statistical quantification of microstructures from microscopy images of polycrystalline nickel based superalloys. *Integr Mater Manuf Innov*, 11(3): 313–326
17. Tiley JS, Viswanathan GB, Shiveley A et al (1993) Measurement of gamma' precipitates in a nickel-based superalloy using energy-filtered transmission electron microscopy coupled with automated segmenting techniques. *Micron Oxford England* 41(2010):641–647
18. Mao J, Chang K-M, Yang W et al (2001) Cooling precipitation and strengthening study in powder metallurgy superalloy U720LI. *Metall Mater Trans A* 32:2441–2452
19. Wusatowska-Sarnek AM, Ghosh G, Olson GB et al (2003) Characterization of the microstructure and phase equilibria calculations for the powder metallurgy superalloy IN100. *J Mater Res* 18:2653–2663
20. Payton EJ, Phillips PJ, Mills MJ (2010) Semi-automated characterization of the phase in Ni-based superalloys via high-resolution backscatter imaging. *Mater Sci Eng, A* 527:2684–2692
21. Chen YQ, Slater TJA, Lewis EA et al (2014) Measurement of size-dependent composition variations for gamma prime (γ') precipitates in an advanced nickel-based superalloy. *Ultramicroscopy* 144:1–8
22. Tang S, Zheng Z, Ning LK (2014) Gamma prime coarsening in a nickel base single crystal superalloy. *Mater Lett* 128:388–391
23. Mallikarjuna HT, Caley WF, Richards NL (2019) The dependence of oxidation resistance on gamma prime intermetallic size for superalloy IN738LC. *Corros Sci* 147:394–405
24. Katsari C-M, Katnagallu S, Yue S (2020) Microstructural characterization of three different size of gamma prime precipitates in Rene 65. *Mater Charact* 169:110542
25. MacSleynne JP, Simmons JP, Graef M, de, (2008) On the use of 2-D moment invariants for the automated classification of particle shapes. *Acta Mater* 56:427–437
26. Holzinger M, Schleifer F, Glatzel U et al (2019) Phase-field modeling of γ' -precipitate shapes in nickel-base superalloys and their classification by moment invariants. *European Phys J, B*, 92: 1–9
27. Schleifer F, Müller M, Lin Y-Y et al (2022) Consistent quantification of precipitate shapes and sizes in two and three dimensions using central moments. *Integr Mater Manuf Innov* 11:159–171
28. Guo Z., Song Z., Huang D. et al. 2022 Matrix channel width evolution of single crystal superalloy under creep and thermal mechanical fatigue: experimental and modeling investigations. *Metals Mater Int*
29. Ahmed M, Horst OM, Obaia A et al (2021) Automated image analysis for quantification of materials microstructure evolution. *Modell Simul Mater Sci Eng* 29:55012
30. Yao Z, Degnan CC, Jepson MAE et al (2013) Effect of rejuvenation heat treatments on gamma prime distributions in a Ni based superalloy for power plant applications. *Mater Sci Technol* 29:775–780
31. Horst OM, Rutttert B, Bürger D et al (2019) On the rejuvenation of crept Ni-Base single crystal superalloys (SX) by hot isostatic pressing (HIP). *Mater Sci Eng, A* 758:202–214
32. Tonks MR, Aagesen LK (2019) The phase field method: meso-scale simulation aiding material discovery. *Annu Rev Mater Res* 49:79–102
33. Mikula J, Ahluwalia R, Laskowski R et al (2021) Modelling the influence of process parameters on precipitate formation in powder-bed fusion additive manufacturing of IN718. *Mater Des* 207:109851
34. Böttger B, Apel M, Jokisch T et al (2020) Phase-field study on microstructure formation in Mar-M247 during electron beam welding and correlation to hot cracking susceptibility. *IOP Conf Series Mater Sci Eng* 861:12072
35. Fleck M, Querfurth F, Glatzel U (2017) Phase field modeling of solidification in multi-component alloys with a case study on the Inconel 718 alloy. *J Mater Res* 32:4605–4615
36. Fleck M, Schleifer F, Holzinger M et al. (2021) Phase-field modeling of precipitation microstructure evolution in multicomponent alloys during industrial heat treatments. In: U Reisgen, D Drummer, H Marschall (Hrsg.), *Enhanced material, parts optimization and process intensification, lecture notes in mechanical engineering*. Springer International Publishing, Cham, 70–78.
37. Fleck M, Schleifer F, Holzinger M et al (2018) Phase-field modeling of precipitation growth and ripening during industrial heat treatments in Ni-base superalloys. *Metall Mater Trans A* 49:4146–4157
38. Böttger B, Altenfeld R, Laschet G et al (2018) An ICME process chain for diffusion brazing of alloy 247. *Integr Mater Manuf Innov* 7:70–85
39. Eiken J (2012) Numerical solution of the phase-field equation with minimized discretization error. *IOP Conf Series Mater Sci Eng* 33:12105
40. Finel A, Le Bouar Y, Dabas B et al (2018) Sharp phase field method. *Phys Rev Lett* 121:25501
41. Fleck M, Schleifer F (2022) Sharp phase-field modeling of isotropic solidification with a super efficient spatial resolution. *Eng Comput*
42. Pollock TM, Tin S (2006) Nickel-based superalloys for advanced turbine engines: chemistry, microstructure and properties. *J Propul Power* 22:361–374
43. Fleischmann E, Konrad C, Preußner J et al (2015) Influence of solid solution hardening on creep properties of single-crystal nickel-based superalloys. *Metall Mater Trans A* 46:1125–1130
44. Fleischmann E, Miller MK, Affeldt E et al (2015) Quantitative experimental determination of the solid solution hardening potential of rhenium, tungsten and molybdenum in single-crystal nickel-based superalloys. *Acta Mater* 87:350–356
45. Matan N, Cox DC, Rae C et al (1999) On the kinetics of rafting in CMSX-4 superalloy single crystals. *Acta Mater* 47:2031–2045
46. Sass V, Glatzel U, Feller-Kniepmeier M (1996) Anisotropic creep properties of the nickel-base superalloy CMSX-4. *Acta Mater* 44:1967–1977
47. Harris K, Erickson GL, Sikkenga SL et al (1993) Development of two rhenium-containing superalloys for single-crystal blade and directionally solidified vane applications in advanced turbine engines. *J Mater Eng Perform* 2:481–487
48. Schleifer F, Fleck M, Holzinger M et al. (2020) Phase-field modeling of γ' and γ'' precipitate size evolution during heat treatment of Ni-based superalloys. In: S Tin, MC Hardy, J Clews, et al. (eds), *Superalloys 2020*. Springer International Publishing, Cham, 500–508
49. Pollock TM, Argon AS (1988) Intermediate temperature creep deformation in cmsx-3 single crystals. In: *Superalloys 1988 (sixth international symposium)*. TMS, 285–294.
50. Caron P, Khan T (1983) Improvement of Creep strength in a nickel-base single-crystal superalloy by heat treatment. *Mater Sci Eng* 61:173–184

51. Konrad CH, Brunner M, Kyrgyzbaev K et al (2011) Determination of heat transfer coefficient and ceramic mold material parameters for alloy IN738LC investment castings. *J Mater Process Technol* 211:181–186
52. Andersson J-O, Helander T, Höglund L et al (2002) Thermo-Calc & DICTRA, computational tools for materials science. *Calphad* 26:273–312
53. Fleischmann E (2013) Einfluss der Mischkristallhärtung der Matrix auf die Kriechbeständigkeit einkristalliner Nickelbasis-Superlegierungen, Berichte aus der Materialwissenschaft. Shaker, Aachen
54. Badrinarayanan V, Kendall A, Cipolla R (2017) SegNet: a deep convolutional encoder-decoder architecture for image segmentation. *IEEE Trans Pattern Anal Mach Intell* 39:2481–2495
55. Stan T, Thompson ZT, Voorhees PW (2020) Optimizing convolutional neural networks to perform semantic segmentation on large materials imaging datasets: X-ray tomography and serial sectioning. *Mater Charact* 160:110119
56. ACCESS e.V.; MICRESS[®]; accessible at: micress.rwth-aachen.de /; Accessed: 01.01.2022.
57. Böttger B, Apel M, Budnitski M et al (2020) Calphad coupled phase-field model with mechano-chemical contributions and its application to rafting of γ' in CMSX-4. *Comput Mater Sci* 184:109909
58. Eiken J, Böttger B, Steinbach I (2006) Multiphase-field approach for multicomponent alloys with extrapolation scheme for numerical application. *Phys Rev E Statistical Nonlinear Soft Matter Physics* 73:66122
59. Böttger B, Eiken J, Apel M (2015) Multi-ternary extrapolation scheme for efficient coupling of thermodynamic data to a multi-phase-field model. *Comput Mater Sci* 108:283–292
60. Fleck M, Schleifer F, Holzinger M et al. 2019 Improving the numerical solution of the phase-field equation by the systematic integration of analytic properties of the phase-field profile function. In: 8th GACM colloquium. Kassel University Press, (2019) 445–450.
61. Lorensen WE, Cline HE (1987) Marching cubes: a high resolution 3D surface construction algorithm. *ACM SIGGRAPH Comput Graphics* 21:163–169
62. Li B (1993) The moment calculation of polyhedra. *Pattern Recogn* 26:1229–1233
63. Sheynin SA, Tuzikov AV 2001 Formulae for polytope volume and surface moments. In: Proceedings 2001 international conference on image processing (Cat. No.01CH37205). IEEE, Thessaloniki, Greece, 720–723.
64. Sheynin SA, Tuzikov AV (2001) Explicit formulae for polyhedra moments. *Pattern Recogn Lett* 22:1103–1109
65. van Rossum G, Drake Jr FL, Python tutorial; The Netherlands: Centrum voor Wiskunde en Informatica, Heft 620, Amsterdam, (1995).
66. Virtanen P, Gommers R, Oliphant TE et al (2020) SciPy 1.0: fundamental algorithms for scientific computing in Python. *Nat Methods* 17:261–272
67. Harris CR, Millman KJ, van der Walt SJ et al (2020) Array programming with NumPy. *Nature* 585:357–362
68. Pedregosa F, Varoquaux G, Gramfort A et al (2011) Scikit-learn: machine learning in python. *J Mach Learn Res* 12:2825–2830
69. Reback J., jbrockmendel, McKinney W. et al.; pandas-dev/pandas: Pandas 1.4.3. Zenodo. 2022.
70. McKinney W (2010) Data structures for statistical computing in python. In: Proceedings of the 9th python in science conference. SciPy, Austin, Texas, 56–61.
71. Sullivan C, Kaszynski A (2019) PyVista: 3D plotting and mesh analysis through a streamlined interface for the visualization toolkit (VTK). *J Open Source Softw* 4:1450

Publisher's Note Springer Nature remains neutral with regard to jurisdictional claims in published maps and institutional affiliations.